Methane and Carbon Dioxide in Dual-Porosity Organic Matter: Molecular Simulations of Adsorption and Diffusion

Eliška Rezlerová[1,2], John K. Brennan[3] and Martin Lísal[1,2]

April 6, 2020

[1] *Department of Molecular and Mesoscopic Modelling, The Czech Academy of Sciences, Institute of Chemical Process Fundamentals, Prague, Czech Republic*

[2] *Department of Physics, Faculty of Science, J. E. Purkinje University, Ústí n. Lab., Czech Republic*

[3] *Weapons and Materials Research Directorate, U.S. Army Combat Capabilities Development Command Army Research Laboratory, Aberdeen Proving Ground, MD, USA*

*Corresponding author: lisal@icpf.cas.cz

Mailing address: Department of Molecular and Mesoscopic Modelling, The Czech Academy of Sciences, Institute of Chemical Process Fundamentals, Rozvojová 135/1, 165 02 Prague 6-Suchdol, Czech Republic

Shale gas, which predominantly consists of methane, is an important unconventional energy resource that has had a potential game-changing effect on natural gas supplies worldwide in recent years. Shale is comprised of two distinct components: organic material and clay minerals, the former providing storage for hydrocarbons and the latter minimizing hydrocarbon transport. The injection of carbon dioxide in the exchange of methane within shale formations improves the shale gas recovery, and simultaneously sequesters carbon dioxide to reduce greenhouse gas emissions. Understanding the properties of fluids such as methane and methane/carbon dioxide mixtures in narrow pores found within shale formations is critical for identifying ways to deploy shale gas technology with reduced environmental impact. In this work, we apply molecular-level simulations to explore adsorption and diffusion behavior of methane, as a proxy of shale gas, and methane/carbon dioxide mixtures in realistic models of organic materials. We first use molecular dynamics simulations to generate the porous structures of mature and overmature type-II organic matter with both micro- and mesoporosity, and systematically characterize the resulting dual-porosity organic-matter structures. We then employ the grand canonical Monte Carlo technique to study the adsorption of methane and the competing adsorption of methane/carbon dioxide mixtures in the organic-matter porous structures. We complement the adsorption studies by simulating the diffusion of adsorbed methane, and adsorbed methane/carbon dioxide mixtures in the organic-matter structures using molecular dynamics.

Keywords: CO_2 sequestration; grand canonical Monte Carlo; molecular dynamics; shale formation; shale gas recovery

1 Introduction

Shale gas, which predominantly consists of methane, is an unconventional energy source that is expected to play an imminent role in the energy market of the immediate future [1]. Shale rocks are composed of organic and inorganic matter with pore sizes ranging from the nano- to the mesoscale. The organic matter (OM) provides storage for hydrocarbons, while the inorganic matter (clay minerals) minimizes hydrocarbon transport. The OM is primarily comprised of kerogen, but it also contains other compounds such as resins, asphaltenes and heavy hydrocarbons. In shale formations, shale gas is stored as free gas in fractures and macropores, as adsorbed gas on pore surfaces and nanopores, and as dissolved gas in the OM. The sorption amount of the gas depends largely on the total organic carbon (TOC) content [2].

Carbon dioxide exhibits a stronger interaction with shale pore surfaces than methane, where this preferential adsorption of CO_2 over CH_4 plays the key role in displacing adsorbed shale gas. On the other hand, due to the stronger CO_2 interaction, the diffusion of carbon dioxide in shale pores is lower in comparison with methane, which may limit the displacement of the adsorbed shale gas [3]. As such, enhanced shale gas recovery with CO_2 injection is a promising technique as it combines the advantages of improving the efficiency of shale gas recovery, and reducing greenhouse gas emissions by geological sequestration of carbon dioxide [4].

Understanding the properties of fluids such as methane and methane/carbon dioxide mixtures in the narrow shale pores is critical for identifying ways to deploy shale gas technology with reduced environmental impact. Laboratory experiments such as the adsorption-desorption method [5], the differential scanning calorimetry method [6], the diffusion method [7], and the nanochannel chips method [8] can provide only limited information about the adsorption and diffusion behavior of fluids in shale pores because typically the experiments are performed under low to medium temperatures and pressures, which differ from realistic reservoir conditions [9]. Molecular-level simulations are important alternatives and complementary tools to experimental measurements since they can provide detailed information about the microscopic mechanism of the gas adsorption/desorption and diffusion processes in the shale matrix at realistic reservoir conditions [10]. Simulation methods for modeling gas adsorption and diffusion in porous materials are well established, which include grand canonical Monte Carlo (GCMC), molecular dynamics (MD) [11, 12], and hybrid GCMC-MD techniques such as dual control volume grand canonical MD [13].

The level of realism of molecular simulations of shale gas adsorption and diffusion critically

depends on building representative models of the shale matrix. Kerogen, which is a main component of the OM, represents a complex material composed of an amorphous porous carbon skeleton, and exhibits significant pore-shape and pore-connectivity variations. The van Krevelen diagram (Fig. 1a), which is a plot of hydrogen-to-carbon (H/C) and oxygen-to-carbon (O/C) atomic ratios, provides a tool to distinguish different types of kerogen in terms of maturity and depositional origin (in parenthesis): type I (lacustrine), type II (marine), type III (terrestrial), and type IV (originating from residues) [14, 15].

Kerogen and its pores can be modelled by (i) constitutive, (ii) mimetic, (iii) reconstruction, and (iv) representative molecular models [16]. The constitutive models include graphitic slit pores and cylindrical pores, such as carbon nanotubes [17, 18, 19]. The mimetic models are built using reactive force fields and quenched MD [20, 21]. The reconstruction models also employ reactive force fields along with a MD-hybrid reverse Monte Carlo method to generate kerogen models by matching experimental and simulated structural properties, such as C-C pair distribution functions [22, 23]. The representative molecular models involve the construction of a model molecule of kerogen based on available experimental data (elemental analysis and scattering data), and prior knowledge of the molecular fragments that likely exist in kerogen. The latter models were pioneered by Ungerer et al. [24] who published a number of kerogen molecules/fragments of smaller sizes, which represented different kerogen types at different maturation stages, and constructed them using experimental data [25] and prior knowledge about the molecular fragments. Most kerogen models neglect the effect of adsorption-induced deformations by considering kerogen as a rigid, non-deformable matrix [26]. However, flexible kerogen models have been considered, where they exhibited an increase in gas diffusivity with respect to rigid kerogens due to fluctuations in the pore connectivity [27, 28, 29, 30]. Due to their robust properties, the representative molecular models have become a preferential approach for modeling shale matrices with a broad diversity of physical properties such as TOC, density, porosity and permeability, as demonstrated by the growing number of molecular simulation studies found in the literature. For example, Collell et al. [31] performed MD simulations of hydrocarbons permeating through oil-prone type II kerogen, and found the permeation mechanism is purely diffusive. Michalec and Lísal [3], and Vasileiadis et al. [32] simulated adsorption and diffusion of various proxies of shale gas along with CO_2 in overmature type II kerogens with control microporosity. The microporosity was introduced into the kerogen structures by dummy particles of various size to mimic neglected compounds in real OM. In another study, Ho et al. [33] showed that methane release in nanoporous kerogen matrices is characterized by a fast release of pressurised free gas (accounting for less than 50 %

recovery), followed by a slow release of adsorbed gas as the gas pressure decreases. There are still other related molecular-level simulation studies on enhanced shale gas recovery by carbon dioxide and CO_2 sequestration in kerogen matrices of different maturity and porosity, see e.g. [34, 35, 36, 37, 38, 39].

Most molecular models treat the shale OM as a dense porous kerogen matrix [9, 10]. Although kerogen is the abundant species in the OM, the OM also contains other compounds such as asphaltenes, resins, and dissolved species (typically hydrocarbons, water and carbon dioxide), where their absence may be mimicked by introducing dummy particles into the kerogen matrix [3, 26]. An exception is the work by Collell et al. [40] who generated the molecular model of type II OM corresponding to midway through the oil formation process. Based on experimental composition data [2], they generated the OM structure by gradually cooling and compressing the initial low-density random configurations, which contained the representative molecular model of type II kerogen, asphaltene/resin, hydrocarbons, water, and carbon dioxide. The kerogen taken together with the other species provides a more faithful representation of OM with an intrinsic microporous network, as compared to models with solely kerogen.

In this work, we used Collell et al.'s approach [40], and generated two realistic models of a type II OM microporous structure by MD simulation: (i) a mature OM corresponding to the oil formation process; and (ii) an overmature OM corresponding to the gas formation process; see the van Krevelen diagram in Fig. 1a. We then introduced mesoporosity into the OM models by separating the OM microporous structures by a distance of 20 or 30 Å, creating a slit-shaped mesopore with a width corresponding to these distances. This was followed by GCMC simulations of the adsorption behavior of pure methane and equimolar methane/carbon dioxide mixtures in the dual-porosity OM structures. We evaluated the adsorption amount separately in the microporous matrix and the mesopore slit to assess adsorption capacity due to the microporosity and mesoporosity [41]. Equilibrium concentrations from GCMC simulations were then employed in MD simulations to evaluate self-diffusivity of adsorbed methane and carbon dioxide along the adsorption isotherms to provide insight into the interplay between gas adsorption and gas diffusion, and into the molecular mechanism for the potential replacement of adsorbed shale gas by carbon dioxide in the shale OM. The remainder of the paper is organized as follows. Section 2 outlines the generation of the dual-porosity OM structures along with the molecular models and simulation details. In Section 3, we then present and discuss our results on the structure characterization of the OM models, and on the adsorption and molecular diffusion of methane and methane/carbon dioxide

mixtures in the OM structures. Finally, we give our conclusions in Section 4.

2 Models and Methodology

2.1 Dual-Porosity Organic Matter

Most of the previous molecular-level simulation studies on the adsorption and diffusion of shale gas approximated the OM by dense porous kerogen matrices, while neglecting the presence of other compounds. However, such an approximation holds only for immature OM, which is almost exclusively comprised of immature kerogen. At the early stages of the maturation process of sedimentary OM, carbon dioxide, water, and asphaltene/resin molecules are produced. Then during the later stages of maturation, alkyl chains and cyclics are generated along with a minor fraction of alkanes and aromatics, leading first to crude oils, and then to gases [2, 42].

Here, we consider mature and overmature type II OM, whereby following Collell et al. [40], we assume that the OM are comprised of the kerogen fraction, asphaltene/resin fraction, hydrocarbon fraction, and carbon dioxide/water fraction. Compositions of the OM are based on the experimental data of Tissot and Welte [2], and Kelemen et al. [25], where it is assumed that the atomic balance is preserved during the maturation process. The latter is equivalent to considering that the compounds generated during the diagenesis and catagenesis processes have not been expelled, and that CO_2 has been preserved from reacting with the inorganic matrix. Finally, the distribution of the hydrocarbon fraction corresponds to a typical condensate gas [43].

In the van Krevelen diagram (Fig. 1a), the mature and overmature kerogens are indicated by stars. The mature kerogen fragment has a chemical formula $C_{242}H_{219}O_{13}S_2N_5$, a molecular weight $M_w = 3468.4$ g/mol, and has a significantly folded structure. The overmature kerogen fragment has a chemical formula $C_{175}H_{102}O_9S_2N_4$, $M_w = 2468.9$ g/mol, and exhibits a flat and rigid structure. The molecular models of both kerogen fragments are shown in Figs. 1b and 1c. The asphaltene/resin fraction corresponds to the hydrocarbon compounds, which are made up of polyaromatic units of lower molecular weight compared to the kerogen. The asphaltene/resin fraction was represented by a generic molecular model with a chemical formula $C_{26}H_{32}O$ and $M_w = 360.5$ g/mol [44]. The hydrocarbon fraction was represented by eight compounds lumped together: six paraffins (C_1 to C_4, C_8 and C_{14}) and two representative aromatic compounds (toluene and dimethylnaphtalene) [40, 43]. In addition, both the mature and overmature OM models contain carbon dioxide and water. The compositions of the OM

structures considered in this study are provided in Table S1 of the Supplementary Material along with simulation details to generate the model OM structures.

2.2 Molecular Models

We modeled the kerogen fragments, asphaltene/resin molecules, hydrocarbons, water and carbon dioxide using a non-polarizable all-atom force field with the functional form [45]

$$\begin{aligned} U &= U_{\text{bonded}} + U_{\text{non-bonded}} \\ &= \sum_{\text{bonds}} \frac{k_b}{2}\left(b - b_0\right)^2 + \sum_{\text{angles}} \frac{k_\theta}{2}\left(\theta - \theta_0\right)^2 + \sum_{\text{dihedrals}} k_\phi\left[1 + \cos\left(n_\phi \phi\right)\right] \\ &+ \sum_{\text{impropers}} k_\psi\left[1 + \cos\left(n_\psi \psi\right)\right] + \sum_i \sum_{j>i} \left\{ 4\varepsilon_{ij}\left[\left(\frac{\sigma_{ij}}{r_{ij}}\right)^{12} - \left(\frac{\sigma_{ij}}{r_{ij}}\right)^{6}\right] + \frac{q_i q_j e^2}{4\pi\epsilon_0 r_{ij}} \right\} \end{aligned} \tag{1}$$

where b, θ, ϕ and ψ denote the bond length, bond angle, dihedral angle and improper angle, respectively; b_0 and θ_0 are the equilibrium bond length and bond angle, respectively; k_b, k_θ, k_ϕ and k_ψ are the force constants; n_ϕ and n_ψ are the dihedral and improper angle parameters, respectively; ε_{ij} and σ_{ij} correspond to the Lennard-Jones (LJ) energy and size parameters, respectively; q_k is the partial charge on atom k, e is the elementary charge, ϵ_0 is the permittivity in vacuum, and r_{ij} is the distance between atoms i and j.

For the kerogen fragments and asphaltene/resin molecules, we used the Consistent Valence Force Field (CVFF) [46], which is a standard and reliable force field for simulation of organic molecules. For the hydrocarbons, water, and carbon dioxide, we employed the Optimized Potential for Liquid Simulations (OPLS) [47], the flexible Extended Simple Point Charge (SPC/E) [48, 49], and the flexible Elementary Physical Model (EPM2) [50] force fields, respectively. The OPLS, SPC/E, and EPM2 force fields have been shown to satisfactorily reproduce the thermodynamic and vapor-liquid equilibrium properties [51, 52, 53], additionally, the force fields are compatible with the CVFF [46]. The LJ cross-interactions were given by the Lorentz-Berthelot combining rules [11]: $\varepsilon_{ij} = \sqrt{\varepsilon_{ii}\varepsilon_{jj}}$ and $\sigma_{ij} = \left(\sigma_{ii} + \sigma_{jj}\right)/2$. For the values of the LJ parameters and the partial charges, we refer the reader to the original papers [46, 47, 48, 49, 50].

2.3 Grand Canonical Monte Carlo

In the first part of this study, we consider the equilibrium behavior between the bulk-like free gas found in the shale macropores and the adsorbed gas in the OM structure. The free gas is either pure methane or equimolar mixtures of methane and carbon dioxide. The equilibrium

between these two phases, i.e., the equivalence of the chemical potentials of the gas species was established using GCMC [11, 12]. In the GCMC simulations, we consider a porous material at constant volume (the OM structure with kerogen fragments, asphaltene/resin molecules, and other dissolved species) in equilibrium with a gas reservoir (the bulk methane phase or bulk methane/carbon dioxide mixture phase) at temperature, T, and pressure, P. The reservoir imposes the chemical potentials, $\mu_i(T, P)$, where their values are inputs to the GCMC simulation. We determined the value of μ_i by the Widom's insertion method [54] using isothermal-isobaric Monte Carlo (NPT MC) simulations of the bulk phase. For a given μ_i and T, the amount adsorbed is then given by the ensemble average of the number of adsorbed gas molecules in the OM structure. The adsorption isotherm was traced by increasing the pressure, where μ_i determined in the corresponding NPT MC was imposed in the GCMC simulations. Additional simulation details regarding the GCMC simulations are provided in the Supplementary Material.

2.4 Molecular Dynamics

NVT and NPT MD simulations [11, 12] were used to perform the step-wise compression-cooling protocol for generating the microporous OM matrix described in Section 2.1. Further, NVT MD simulations were used to evaluate the diffusion of the states along the adsorption isotherms, where the equilibrium amounts of the adsorbed gases were determined from the GCMC simulations. Additional simulation details regarding the MD simulations are given in the Supplementary Material.

The in-plane diffusion of the adsorbed gas molecules CH_4 and CO_2 was described by the self-diffusivity, D_α, $\alpha \equiv (CH_4, CO_2,)$, which was calculated using the Einstein equation from the mean-square displacement (MSD) parallel to the slit xy-plane, i.e.,

$$\mathrm{MSD}^{\alpha}_{\mathrm{xy}}\left(\mathrm{t}\right) \propto 4\mathrm{D}_{\alpha}\mathrm{t} \tag{2}$$

In Eq. (2), $\mathrm{MSD}^{\alpha}_{\mathrm{xy}}\left(\mathrm{t}\right) \equiv \mathrm{MSD}^{\alpha}_{\mathrm{x}}\left(\mathrm{t}\right) + \mathrm{MSD}^{\alpha}_{\mathrm{y}}\left(\mathrm{t}\right)$, where $\mathrm{MSD}^{\alpha}_{\mathrm{x}}\left(\mathrm{t}\right)$ and $\mathrm{MSD}^{\alpha}_{\mathrm{y}}\left(\mathrm{t}\right)$ are the MSDs in the x- and y-directions at time t, respectively. The determination of the MSDs includes averaging over different time origins [11, 12]. To estimate the time interval for fitting the values of D_α according to Eq. (2), we first evaluated the slope of the MSD

$$\beta\left(t\right) = \frac{\mathrm{d}\ln\left[\mathrm{MSD}^{\alpha}_{\mathrm{xy}}\left(\mathrm{t}\right)\right]}{\mathrm{d}\ln\mathrm{t}} \tag{3}$$

as a function of time t, and selected a time interval over which $\beta\left(t\right) \simeq 1$, which corresponds to normal (Fickian) diffusion [55, 56].

In addition to determining the overall self-diffusivity D_α, we also evaluated D_α limited to either the microporous matrix or the mesopore slit, as described in Refs. [55, 56, 57]. The overall MSD is related to the MSDs in the microporous matrix and the mesopore slit as

$$\mathrm{MSD}^{\alpha}_{\mathrm{xy}}\left(\mathrm{t}\right) = \mathrm{x}^{\mathrm{micro}}_{\alpha}\mathrm{MSD}^{\alpha}_{\mathrm{xy,micro}}\left(\mathrm{t}\right) + \mathrm{x}^{\mathrm{meso}}_{\alpha}\mathrm{MSD}^{\alpha}_{\mathrm{xy,meso}}\left(\mathrm{t}\right) \tag{4}$$

where $x^{\mathrm{micro}}_{\alpha}$ and $x^{\mathrm{meso}}_{\alpha}$ are the compositions of species α in the microporous matrix and the mesopore slit, respectively, and $\mathrm{MSD}^{\alpha}_{\mathrm{xy,micro}}\left(\mathrm{t}\right)$ and $\mathrm{MSD}^{\alpha}_{\mathrm{xy,meso}}\left(\mathrm{t}\right)$ are the MSDs of species α in the microporous matrix and mesopore slit at t, respectively. For normal diffusion

$$D_\alpha = x^{\mathrm{micro}}_{\alpha} D^{\mathrm{micro}}_{\alpha} + x^{\mathrm{meso}}_{\alpha} D^{\mathrm{meso}}_{\alpha} \tag{5}$$

where $D^{\mathrm{micro}}_{\alpha}$ and $D^{\mathrm{meso}}_{\alpha}$ are the self-diffusivities in the microporous matrix and the mesopore slit, respectively, evaluated using the Einstein equation [Eq.(2)].

3 Results and Discussion

The results of the simulation study are presented next. In Section 3.1, the structures of the OM matrices have been characterized based upon the geometric pore size distribution, the accessible surface area, the pore limiting diameter, and the micro- and mesopore volumes. In Sections 3.2 and 3.3, the adsorption and diffusion results are presented, respectively. All of the adsorption and diffusion simulations were performed at temperatures, $T = \{298, 323, 343\}$ K, and pressures, $P = \{50, 100, 275\}$ bar. The temperatures 323 and 343 K together with these pressures represent typical reservoir conditions [58], while the behavior at 298 K corresponds to ambient conditions. The model critical temperature, T_c, and critical pressure, P_c, are $(T_c, P_c) \simeq (191\ \mathrm{K}, 46\ \mathrm{bar})$ for methane and $(T_c, P_c) \simeq (306\ \mathrm{K}, 77\ \mathrm{bar})$ for CO_2 [51, 52], which compare rather well with the experimental values $(T_c, P_c) \simeq (191\ \mathrm{K}, 46\ \mathrm{bar})$ and $(T_c, P_c) \simeq (304\ \mathrm{K}, 74\ \mathrm{bar})$, respectively [59].

3.1 Organic-Matter Structure Characterization

Examples of the dual-porosity OM structures generated from the step-wise compression-cooling strategy are shown in Fig. 2. Visual inspection of the microporous matrix indicates a rather tortuous pore network in the kerogen skeleton of the mature OM structures (Fig. 2a), and a parallel-stacked arrangement in the kerogen skeleton of the overmature OM structures (Fig. 2b). Further, we systematically characterized the OM structures by calculating the geometric pore size distribution (PSD) for the kerogen skeleton, the accessible surface area,

S_{A}, and the pore limiting diameter, D_{min}, of the kerogen in the microporous matrix. Details of these calculations are given next.

The PSD was determined by the following Monte Carlo procedure. A dense lattice of test points was placed in the simulation box and then the entire micropore space was probed by finding the largest spheres that contained test points, but did not overlap with the kerogen atoms. Each sphere then defined the volume of a void space that can be covered by a sphere of radius r or smaller, $V_p(r)$. The derivative $-\mathrm{d}V_p/\mathrm{d}r$ is the PSD, which was obtained by numerical differentiation of $V_p(r)$ [60, 61]. The PSDs for both of the OM structures are displayed in Fig. 2, where two distinct pore size regions are evident in all of the structures. The PSDs have a broad distribution of ultramicropores up to micropores, which are wider for the overmature OM structures (Fig. 2b) compared to the mature OM structures (Fig. 2a). Further, the PSDs exhibit a pronounced distribution of large micropores up to mesopores, the latter corresponding to the mesopore slit and its confining corrugated wall surfaces.

The accessible surface in the microporous matrix was obtained as a locus of the points that represents the location of the probe particle at a distance of the collision diameter σ from any atom in the microporous structure. A nitrogen atom with $\sigma_{\mathrm{N}} = 3.314$ Å was used as a probe particle to directly relate the calculated S_{A} to that measured in BET adsorption experiments [3]. Application of the PoreBlazer tool [61] predicts $S_{\mathrm{A}} \simeq 125$ and 175 m^2/g for the mature and overmature kerogen in the microporous matrix. These values can be compared with $S_{\mathrm{A}} \simeq 95$ m^2/g for the mature type II OM structures by Collell et al. [31], and with $S_{\mathrm{A}} \simeq \{40, 75, 130, 150\}$ m^2/g for the overmature type II kerogen structures by Michalec and Lísal [3], generated using LJ dummy particles with the size $\sigma_{\mathrm{LJ}} = \{9, 11, 13, 15\}$ Å.

The pore limiting diameter of the kerogen in the microporous matrix corresponds to a maximum probe size for which a pore network percolates. Application of the PoreBlazer tool [61] yields $D_{\mathrm{min}} \simeq 7.8$ and 11.3 Å for the mature and overmature kerogen skeletons, respectively, which indicates that normal diffusion will occur for both methane and carbon dioxide in the microporous matrix. It is worthwhile to mention that in the absence of the asphaltene/resin molecules and the other dissolved species that arise during the generation of the microporous matrix, values of D_{min} would be rather small, and the microporous kerogen would not exhibit percolation for methane and carbon dioxide, unless dummy particles would be used [3, 26].

For methane adsorption in the OM structures (acting here as a proxy for shale gas adsorption), the excess adsorption amount was also computed, which requires determining the pore volume, V_{pore}. We approximated values of V_{pore} from the free volume obtained by the

following Monte Carlo procedure. Using the final equilibrated dual-porosity OM structures, we first performed NVT MD simulations for a few ns, periodically saving approximately a thousand configurations. Then for each of these configurations, we tested if a randomly inserted He-size probe particle with $\sigma_{\mathrm{He}} = 2.58$ Å (viz helium pycnometry) overlapped with any atoms in the OM structure, repeating this overlap test 10^6 times. The fraction of insertions that does not overlap with any OM atom determines the free volume (as a fraction of the simulation box, V_{box}) [62]. We determined the free volume and in turn V_{pore} separately in the microporous matrix and mesopore slit without considering the dissolved methane. The boundary between the microporous and mesopore regions was determined via the Gibbs dividing plane evaluated using the density profile of the kerogen skeleton, see Section 3.2. We obtained $\left(V_{\mathrm{pore}}^{\mathrm{micro}}, V_{\mathrm{pore}}^{\mathrm{meso}}\right) \simeq (0.0276V_{\mathrm{box}}, 0.149V_{\mathrm{box}})$ and $\left(V_{\mathrm{pore}}^{\mathrm{micro}}, V_{\mathrm{pore}}^{\mathrm{meso}}\right) \simeq (0.0244V_{\mathrm{box}}, 0.248V_{\mathrm{box}})$ for the mature OM structures with the 20 Å slit and 30 Å slit, respectively, and $\left(V_{\mathrm{pore}}^{\mathrm{micro}}, V_{\mathrm{pore}}^{\mathrm{meso}}\right) \simeq (0.0460V_{\mathrm{box}}, 0.127V_{\mathrm{box}})$ and $\left(V_{\mathrm{pore}}^{\mathrm{micro}}, V_{\mathrm{pore}}^{\mathrm{meso}}\right) \simeq (0.0416V_{\mathrm{box}}, 0.207V_{\mathrm{box}})$ for the overmature OM structures with the 20 Å slit and 30 Å slit, respectively.

3.2 Adsorption

3.2.1 Methane Adsorption

Fig. 3 presents adsorption isotherms for total and excess adsorption of methane in the OM structures studied. The CH_4 total adsorption corresponds to the entire quantity of methane that resides in the OM structure, which includes both the methane within the micropores and mesopore slit (i.e., free gas), and the methane adsorbed directly on the micropore and mesopore surfaces (i.e., gas in an adsorbed state). The CH_4 excess adsorption is the difference between the total adsorbed amount, n, and the amount of methane in the free volume of the OM micropores and mesopore slit, and characterizes the methane in the adsorbed state. The excess adsorption was estimated as

$$n^{excess} = n - \left(V_{\mathrm{pore}}^{\mathrm{micro}} + V_{\mathrm{pore}}^{\mathrm{meso}}\right) \rho_{TP} \tag{6}$$

where ρ_{TP} is the density of bulk methane at T and P, as obtained by NPT MC simulations.

From Fig. 3, several general trends are evident. First, the adsorption exhibits type-I Langmuir adsorption behavior, where the total adsorption increases with increasing pressure, which is the expected behavior for these materials. (The isotherm at $T = 298$ K in the 20 Å-mature OM structure deviates from this pressure dependence, which is discussed below.) Second, the total adsorption decreases with increasing temperature, where the increase in the mobility (kinetic energy) of the methane molecules overcomes the attraction with the pore

surfaces resulting in less methane layered on the surface. As such, at higher temperature, less efficient packing of methane occurs as more free-gas methane occupies the mesopore volume. Third, the total adsorption increases with increasing size of the mesopore width, which is simply a consequence of an increase in the accessible pore volume. Lastly, the excess adsorption isotherms exhibit less dependence on the pressure, temperature and mesopore width, compared to the total adsorption isotherms. This indicates that the methane molecules prefer to occupy the porous volume, rather than forming layers on the surface.

A comparison of both the total and excess adsorption between the mature (Figs. 3a,c) and overmature (Figs. 3b,d) OM structures indicates stronger methane adsorption in the overmature OM structures, overall by about 50 %. This is primarily due to the larger accessible surface area in the microporous matrix for the overmature OM structures, which results in a relative increase in the excess adsorption amount.

As further insight, the adsorption behavior was evaluated separately in the microporous and mesopore regions of the OM structures. The microporous region corresponds to the microporous matrix, while the mesopore region corresponds to the mesopore slit and its confining corrugated surfaces. Fig. 4 provides examples of these quantities at $T = 298$ and 343 K in the 20 Å-mature and 20 Å-overmature OM structures, where a complete set is provided in Figs. S1 to S4 of the Supplementary Material. Fig. 4 along with Figs. S1 to S4 indicate that the adsorption isotherms in the microporous region have minimal dependence with increasing P, where differences between the total and excess adsorbed amount are rather small with only a weak enhancement upon increasing P. This suggests that the microporous regions are nearly filled with methane for the Ps considered in this study, and accessible adsorption sites are scarce. On the other hand, the total adsorption isotherms, and to a certain extent the excess adsorption isotherms in the mesopore region, exhibit a rather strong dependence with increasing P, where the differences between the total and excess adsorbed amount increase with increasing P. This indicates that methane molecules continue to both fill the mesopore space and adsorb on the mesopore surfaces, which still contain accessible adsorption sites. The assessments of the methane adsorption behavior in Fig. 4 and Figs. S1 to S4 are complemented by Figs. S5 to S8 of the Supplementary Material, which presents the fluid density profiles in the OM structures.

In contrast to the other cases considered in this study, the adsorption behavior at $T = 298$ K in the 20 Å-mature OM structure (Figs. 3a and 4a) exhibits a different pressure dependence, as characterized by a peak at $P \sim 60$ bar in both the overall excess adsorption isotherm and the excess adsorption isotherm in the mesopore region. For this particular temperature

and particular mesopore width, this suggests that the accessible surface in the mesopore region has been saturated with methane molecules at $P \sim 60$ bar. Above this P, adsorption only occurs as free gas above the adsorbed layers. Therefore, as this amount increases with increasing P, then relative to the total amount adsorbed, the excess adsorption amount decreases. Note that the excess adsorption isotherm in the microporous region is independent of P, which indicates that the adsorbed layers have been saturated in the microporous region at $P < 60$ bar. The fluid density profiles in the 20 Å-mature OM structure at $T = 298$ K shown in Fig. S9 of the Supplementary Material, further supports this assessment. For the higher temperatures and other OM structures studied here, we expect that the excess adsorption isotherms will exhibit a peak located at $P > 275$ bar.

3.2.2 Competitive Adsorption of Methane and Carbon Dioxide Mixtures

Fig. 5 presents the adsorption isotherms of the equimolar CH_4/CO_2 mixtures in the 20 Å-mature and 20 Å-overmature OM structures, along with the corresponding selectivity parameter, S_{CO_2}. Fig. S10 in the Supplementary Material displays the analogous results in the 30 Å-mature and 30 Å-overmature OM structures. The selectivity parameter characterizes adsorption selectivity as the ratio of the mole fractions of the two species in the adsorbent relative to the ratio of the mole fractions in the bulk phase. As such, S_{CO_2}, defined as

$$S_{CO_2} = \frac{x_{CO_2}/x_{CH_4}}{y_{CO_2}/y_{CH_4}} \tag{7}$$

is a criterion to assess the relative adsorption preference between CH_4 and CO_2 in a binary mixture. In Eq. (7), x_{CO_2} and x_{CH_4} are the average mole fractions of CO_2 and CH_4 in the adsorbent, while y_{CO_2} and y_{CH_4} are the mole fractions of CO_2 and CH_4 in the bulk phase. A larger adsorption selectivity value, S_{CO_2}, corresponds to a greater preference of CO_2 to adsorb in the porous material compared to CH_4.

The adsorption isotherms in Figs. 5a,b and S10a,b indicate that CO_2 is preferentially adsorbed over CH_4 in all of the OM structures, and at all Ts and Ps studied. The CH_4 adsorption isotherms increase with increasing P, and decrease with increasing T, which is analogous to the pure methane adsorption behavior. Also analogous to the pure methane adsorption behavior, CH_4 adsorption is stronger in the overmature OM structures compared to the mature OM structures. However, in contrast to the pure methane adsorption behavior, the CH_4 adsorption only slightly increases with increasing size of the mesopore width. The CO_2 adsorption isotherms at $T = 298$ K, and to a certain extent those at $T = 323$ K, sharply increase between 50 to 100 bar, which corresponds to the P_c of CO_2. At higher pressures, the

isotherms exhibit a rather weak dependence. On the contrary, the CO_2 adsorption isotherms at $T = 343$ K gradually increase with increasing P. The sharp increase in the CO_2 adsorption is associated with a sharp increase in the bulk density around P_c of CO_2, as evident in Fig. S11 of the Supplementary Material. Fig. S11 displays the bulk isotherms for CO_2 (and also CH_4 for the sake of comparison) at all Ts studied, as obtained by our NPT MC simulations. Similar to methane adsorption, the CO_2 adsorption isotherms at $P > 50$ bar decrease with increasing T, and exhibit a stronger CO_2 adsorption in the overmature OM structures compared to the mature OM structures, overall by about 50 %.

The pressure dependence of S_{CO_2}, displayed in Figs. 5c,d and S10c,d, further emphasizes the preferential adsorption of CO_2 over CH_4. The values of S_{CO_2} range between 2.0-4.0, where the overmature OM structures display higher CO_2 adsorption selectivity compared to the mature OM structures. Our simulated values of S_{CO_2} are within the reported experimental values of 1.9-8.9 [63, 64]. The sharp increase in the CO_2 adsorption isotherms at $T = 298$ and 323 K between 50-100 bar coincides with a corresponding sharp increase in S_{CO_2} with increasing P, peaking around the P_c of CO_2; at higher P, S_{CO_2} gradually decreases. In constrast, the CO_2 adsorption selectivity at $T = 343$ K gradually decreases with increasing P. Above the P_c of CO_2, the CO_2 adsorption selectivity decreases with increasing T, which indicates that the CO_2 adsorption decreases faster than the CH_4 adsorption upon increasing T. However above 200 bar, S_{CO_2} appears to be nearly independent of T.

Fig. 6 and Figs. S12 to S15 of the Supplementary Material detail the preferential adsorption of CO_2 over CH_4 by presenting the adsorption isotherms of the equimolar CH_4/CO_2 mixtures separately in the microporous and mesopore regions of the OM structures. The figures indicate that CO_2 is preferentially adsorbed over CH_4 in both the microporous and mesopore regions. A comparison of the CH_4 and CO_2 adsorption isotherms in the 20 Å-mature and 20 Å-overmature OM structures (Figs. 6, S12 and S13) indicates CH_4 more strongly adsorbs in the mesopore region than in the microporous region in both OM structures, while adsorption in the microporous region marginally increases with P. CO_2 exhibits similar behavior in the 20 Å-mature OM structure. However, in contrast, CO_2 adsorption becomes stronger in the microporous region than in the mesopore region for the 20 Å-overmature OM structure, while CO_2 adsorption in both regions decreases with increasing P. Moreover, as the mesopore width increases to 30 Å (Figs. S14 and 15), adsorption of both CH_4 and CO_2 in the mesopore region increases for the 30 Å-overmature OM structure, while CO_2 adsorption in both the microporous and mesopore regions becomes comparable.

The CH_4 and CO_2 adsorption behavior in the microporous and mesopore regions of the

OM structures is complemented by computing the corresponding values of S_{CO_2}, presented in Figs. S16 to S19 of the Supplementary Material. Values of S_{CO_2} are about 2 in the mesopore regions, while values of nearly 6 are observed in the microporous regions, suggesting that both microporous OM matrices are strong adsorbents for carbon dioxide. Finally, similar to pure methane adsorption, we present fluid density profiles in the OM structures (Figs. S20 to S23 of the Supplementary Material) to further emphasize the preferential adsorption of CO_2 over CH_4 in the OM structures studied.

3.3 Molecular Diffusion

The diffusion of methane molecules, and the competing diffusion of methane and carbon dioxide in OM is critical, respectively, in shale gas transport and enhanced shale gas recovery by carbon dioxide. Generally, confinement hinders the diffusion of the adsorbed molecules inside the micro-, as well as mesopores, and restricts access to the adsorption sites. Diffusion in the porous material is affected by the porous structure (size of pores, pore connectivity and tortuosity), and the affinity of the adsorbates towards the pore surfaces.

3.3.1 Methane Self-Diffusivity

Fig. 7 displays the self-diffusivity of methane, D_{CH_4}, along with the CH_4 adsorption isotherms for all of the OM structures studied. Four general trends are observed. First, D_{CH_4} decreases as P increases due to the increase of CH_4 adsorption with increasing P. Second, D_{CH_4} increases with increasing T due to the increase in the mobility (kinetic energy) of the adsorbed CH_4 molecules with increasing T. Third, due to the stronger CH_4 adsorption in the overmature OM structures compared to the mature OM structures, D_{CH_4} is lower in the overmature OM structures by about 20 %. Finally, D_{CH_4} increases with increasing mesopore width because the CH_4 molecules adsorbed as free gas have a higher mobility in the wider mesopores compared to the narrower mesopores. D_{CH_4} along the adsorption isotherm at $T = 298$ K for the 20 Å-mature OM exhibits a moderately different pattern due to the distinct adsorption behavior discussed above.

To provide further insight into CH_4 diffusion in the OM structures, Fig. 8 presents examples of D_{CH_4} along the adsorption isotherms at $T = 298$ and 343 K in the 30 Å-mature and 30 Å-overmature OM structures, evaluated separately in the microporous and mesopore regions. A complete set of D_{CH_4} along all CH_4 adsorption isotherms is provided in Figs. S24 to S27 of the Supplementary Material. Fig. 8, together with Figs. S24 to S27, as expected, indicate that D_{CH_4} in the mesopore region is enhanced with respect to the overall D_{CH_4}, while D_{CH_4}

in the microporous region is reduced with respect to the overall D_{CH_4}. Furthermore, D_{CH_4} in both regions decreases with increasing P, while increases with increasing T, similar to the overall D_{CH_4}. The enhancement of D_{CH_4} in the mesopore region is about 20 % in both OM structures, which is due to the higher mobility of CH_4 in the centre of the mesopores, where CH_4 molecules behave as free gas. On the other hand, the reduction of D_{CH_4} in the microporous region is more pronounced for the mature OM structures (by about 50 %) than for the overmature OM structures (by about 20 %). Moreover, D_{CH_4} in the microporous region of the overmature OM structures becomes higher than or comparable with D_{CH_4} in the microporous region of the mature OM structures despite the stronger CH_4 adsorption in the microporous overmature OM matrices. This behavior is associated with the parallel-stacked arrangement of the kerogen fragments in the microporous overmature OM matrices, which enhances diffusion when compared with the rather tortuous pore kerogen network in the microporous mature OM matrices.

3.3.2 Self-Diffusivity of Methane and Carbon Dioxide Mixtures

Enhanced shale gas recovery by carbon dioxide injection relies on: (i) the preferential adsorption of CO_2 compared to the shale gas in the shale rock OM; and (ii) sufficient diffusion of the adsorbed CO_2 molecules within the shale rock OM. In Fig. 9, we display the CH_4 and CO_2 self-diffusivity, D_{CH_4} and D_{CO_2} respectively, along the mixture adsorption isotherms for all of the OM structures studied. It is evident that due to the preferential adsorption of CO_2 compared with CH_4, D_{CO_2} is lower than D_{CH_4} by a factor of 3-4 at $P < 100$ bar, and by a factor of about 2 at the higher P. Both D_{CH_4} and D_{CO_2} decrease with increasing P, and increase with increasing T and increasing mesopore width. Note that D_{CH_4} decreases rather rapidly at $P < 100$ bar, which correlates with the sharp increase in the CO_2 adsorption around the P_c of CO_2 (cf. Figs. 5a,b and S10a,b). Both D_{CH_4} and D_{CO_2} in the overmature OM structures are only slightly lower than those in the mature OM structures (by about 10 %), despite both CH_4 and CO_2 adsorbing more strongly in the overmature OM structures compared to the mature OM structures (by about 50 %). Similar to the CH_4 and CO_2 adsorption behavior, this behavior is due to the distinctively different structural characteristics of the porous networks (i.e., the parallel-stacked arrangement of the kerogen fragments for the overmature OM structures compared to the rather tortuous pore kerogen network of the mature OM structures).

To further detail the diffusion of the adsorbed CH_4 and CO_2 molecules in the OM structures, Fig. 10 presents examples of D_{CH_4} and D_{CO_2} along the adsorption isotherms at $T = 298$ and 343 K in the 30 Å-mature and 30 Å-overmature OM structures, evaluated separately

in the microporous and mesopore regions. A complete set of D_{CH_4} and D_{CO_2} along all the adsorption isotherms is provided in Figs. S28 to S31 of the Supplementary Material. It is evident that in the mesopore regions, both D_{CH_4} and D_{CO_2} are enhanced with respect to the overall D_{CH_4} and D_{CO_2} by 20 to 50 %. In the mesopore regions, D_{CH_4} and D_{CO_2} are reduced with respect to the overall D_{CH_4} and D_{CO_2} by a factor of 2-3 for the mature OM structures, and by a factor slightly less than 1 for the overmature OM structures. In both regions, D_{CH_4} and D_{CO_2} decrease with increasing P, and increase with increasing T, similar to the overall D_{CH_4} and D_{CO_2}.

4 Conclusions

We employed molecular dynamics (MD) simulations and generated realistic models of organic matter (OM) structures with both micro- and mesoporosity, which correspond to mature and overmature type-II kerogens. While most previous simulation studies have modeled only the kerogens in the OM structures, in contrast, the model OM structures in this study contain asphaltene/resin, hydrocarbons and carbon dioxide/water fractions. The result of including these other components was a realistic pore network percolation allowing for the diffusion of gas molecules within the microporous matrix of the OM structures. The microporous matrix of the mature OM structures exhibited a rather tortuous pore network in the kerogen skeleton, while the overmature OM structures displayed a parallel-stacked arrangement of kerogen fragments.

To provide molecular-level insight into shale gas adsorption and transport in shale rocks, we evaluated the adsorption and self-diffusivity of methane as a proxy of shale gas using grand canonical Monte Carlo (GCMC) and MD simulations over temperatures and pressures corresponding to typical reservoir conditions. For pure methane in the OM structures, the main findings from our work are:

- The adsorption isotherms exhibit type-I Langmuir adsorption behavior. The total adsorption, and to a certain extent the excess adsorption, increases with increasing pressure as the pressure drives the methane molecules into both the OM micro- and mesopores. Both the total and excess adsorption decreases with increasing temperature due to the increased mobility of the methane molecules, which prefer to behave as free gas in the mesopore rather than adsorb to the pore surfaces.

- The adsorption is higher in the overmature OM structures compared to the mature OM structures, which correlates with the larger accessible surface area of the microporous matrix

in the overmature OM structures. This behavior is also due to the parallel stacking of the kerogen fragments in the overmature OM structures. The latter promotes stronger methane-kerogen surface interactions compared with the tortuous pore network in the mature OM structures.

- The self-diffusivity, D_{CH_4}, along the adsorption isotherms anti-correlates with the adsorption behavior, i.e., D_{CH_4} decreases with pressure, increases with temperature, and is lower in the overmature OM structures than in the mature OM structures.

- Values of D_{CH_4} are reduced in the OM micropores by a factor of about 2 for the mature OM structures, and by a factor of less than 1 for the overmature OM structures, which is associated with the structural characteristics of pore network. The parallel stacking of the kerogen fragments in the overmature OM structures enhances methane diffusion as opposed to the tortuous pore network in the mature OM structures.

To provide molecular-level insight into the displacement of shale gas by carbon dioxide during enhanced shale gas recovery, we further investigated adsorption and self-diffusivity of equimolar methane/carbon dioxide mixtures by GCMC and MD simulations at the relevant reservoir temperatures and pressures. For the equimolar methane/carbon dioxide mixtures in the OM structures, the main findings from our work are:

- CO_2 preferentially adsorbs compared with methane in both of the OM structures studied with a CO_2 selectivity in the range of 2-4. Both the preferential adsorption and selectivity of CO_2 are more pronounced in the overmature OM structures compared to the mature OM structures, which correlates with both the larger accessible surface area of the microporous matrix and the parallel stacking of the kerogen fragments in the overmature OM structures.

- The CH_4 adsorption behavior in the mixture is analogous to the pure methane adsorption behavior. The CO_2 adsorption isotherms are affected by a sharp increase in the bulk density near the CO_2 critical pressure, where the CO_2 adsorption isotherms at temperatures near the CO_2 critical temperature sharply increase, reaching a maximum near the CO_2 critical pressure. Above the CO_2 critical pressure, the CO_2 adsorption isotherms, depending on temperature, either slightly increase or slightly decrease with increasing pressure.

- The CO_2 separation factors at the lower temperatures also exhibit maximums near the CO_2 critical pressure, and then decrease with increasing pressure. The CO_2 separation factors further decrease with increasing temperature, exhibiting faster decrease in the CO_2 adsorption compared with the CH_4 adsorption upon increasing temperature. The CO_2 separation

is significantly enhanced in the micropores with respect to the mesopores, where the CO_2 separation factors may reach values of up to 6.

- Self-diffusivities, D_{CH_4} and D_{CO_2}, along the mixture adsorption isotherms, in general anti-correlate with the mixture adsorption behavior, i.e., D_{CO_2} is lower than D_{CH_4}, depending on pressure, by a factor of 2-4. Both D_{CH_4} and D_{CO_2} decrease with increasing pressure, and increase with increasing temperature. Despite stronger CH_4 and CO_2 adsorption in the overmature OM structures, D_{CH_4} and D_{CO_2} are either only slightly lower than or comparable with those in the mature OM structures. This behavior is due to the enhancement of molecular diffusion by the parallel stacking of the kerogen fragments in the overmature OM structures.

- Values of D_{CH_4} and D_{CO_2} are reduced by a factor of about 3 and by factor of about 1 in the microporous matrix of the mature and overmature OM structures, respectively, reflecting the distinct differences in the structural characteristics of the pore network.

Acknowledgment

This work has received funding from the European Union's Horizon 2020 research and innovation programme under grant agreement No. 640979, ERDF/ESF project "UniQSurf-Centre of biointerfaces and hybrid functional materials" (No. CZ.02.1.01/0.0/0.0/17_048/0007411), and the Internal Grant Agency of J. E. Purkinje University (project No. UJEP-SGS-2019-53-005-3). Access to the computing and storage facilities owned by the parties and projects contributing to the National Grid Infrastructure MetaCentrum provided under the programme "Projects of Large Research, Development, and Innovations Infrastructures" (CESNET LM2015042) is greatly appreciated.

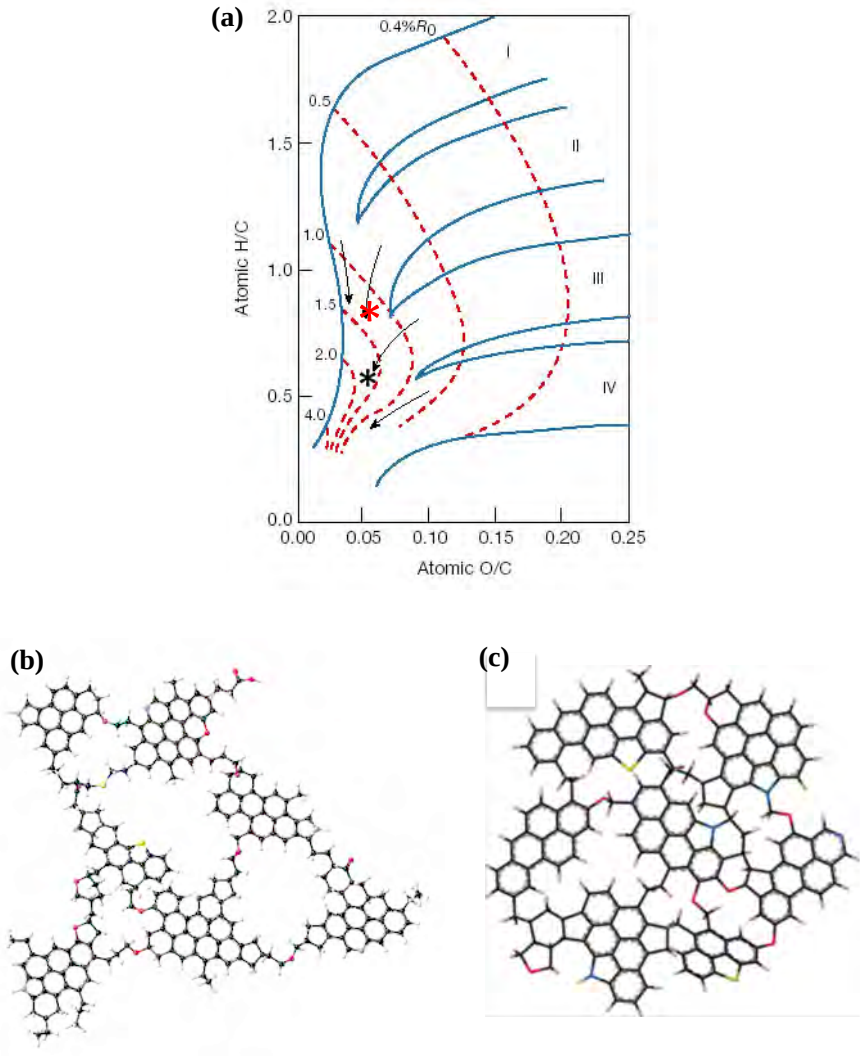

Figure 1: (a) The van Krevelen diagram; R_0 is the vitrinite reflectance [14, 15]. The red and black stars indicate, respectively, the mature and overmature type II kerogens studied in this work. (b) Molecular model of a kerogen unit representing mature type II kerogen. The chemical formula of the kerogen unit is $C_{242}H_{219}O_{13}S_2N_5$, its molecular weight M_w = 3468.4 g/mol, and the atomic ratios are H/C=0.905, O/C=0.054, S/C=0.008 and N/C=0.021. (c) Molecular model of a kerogen unit representing overmature type II kerogen. The chemical formula of the kerogen unit is $C_{175}H_{102}O_9S_2N_4$, its molecular weight M_w = 2468.9 g/mol, and the atomic ratios are H/C=0.58, O/C=0.051, S/C=0.011 and N/C=0.023. The red, blue, yellow, grey and white spheres represent oxygen, nitrogen, sulphur, carbon and hydrogen atoms, respectively. Alternative composition and structural parameters of the kerogen units can be found in Ref. [24].

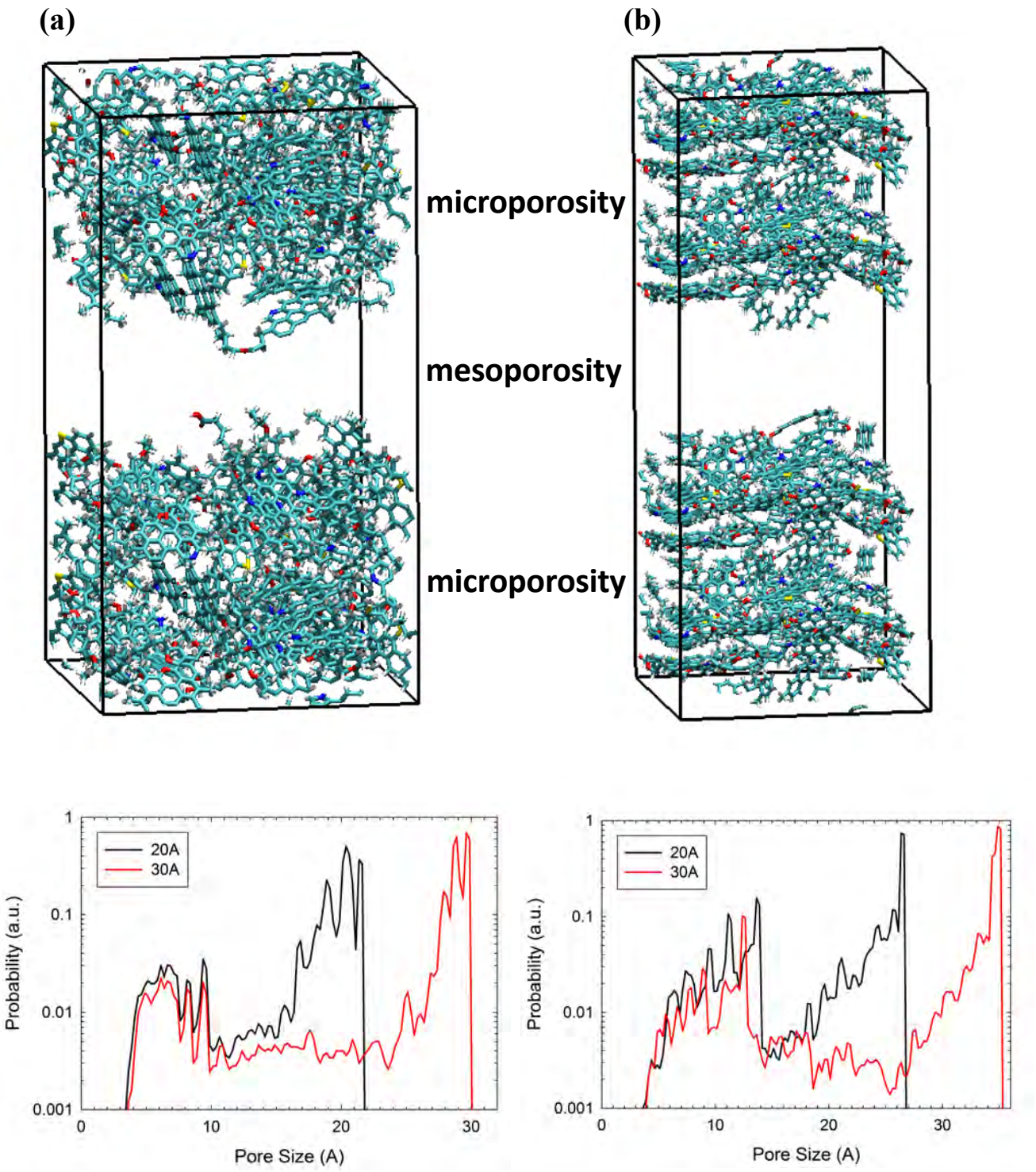

Figure 2: Configuration snapshots (top) and pore size distributions (bottom) for the (a) mature and (b) overmature organic matter structures. For visual clarity, only the kerogen matrix is shown in each snapshot.

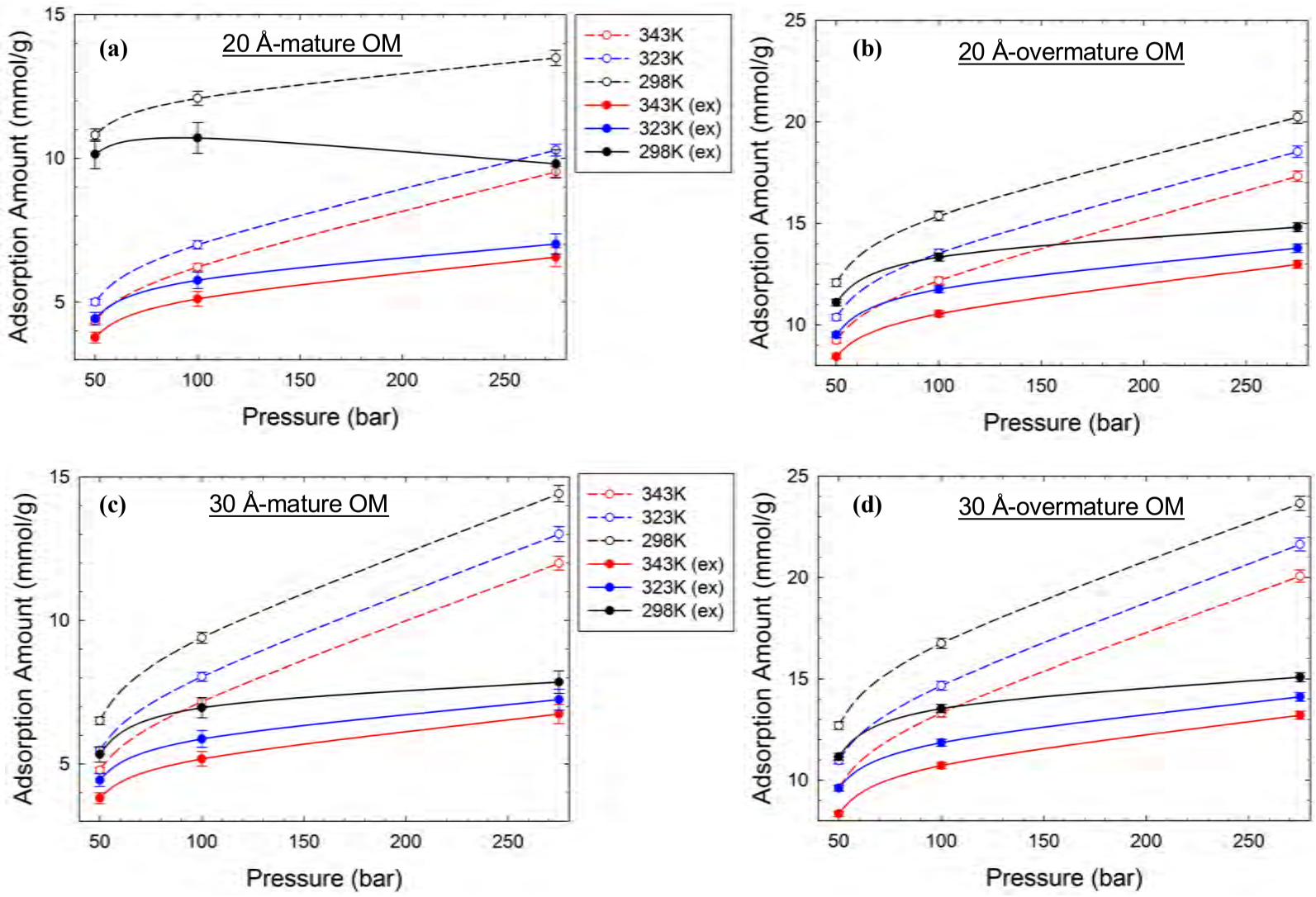

Figure 3: Adsorption isotherms of methane in the mature and overmature organic matter structures. The dashed lines and open symbols denote the total adsorption amount, while the solid lines and filled symbols correspond to the excess adsorption amount. The lines serve as a guide to the eye only.

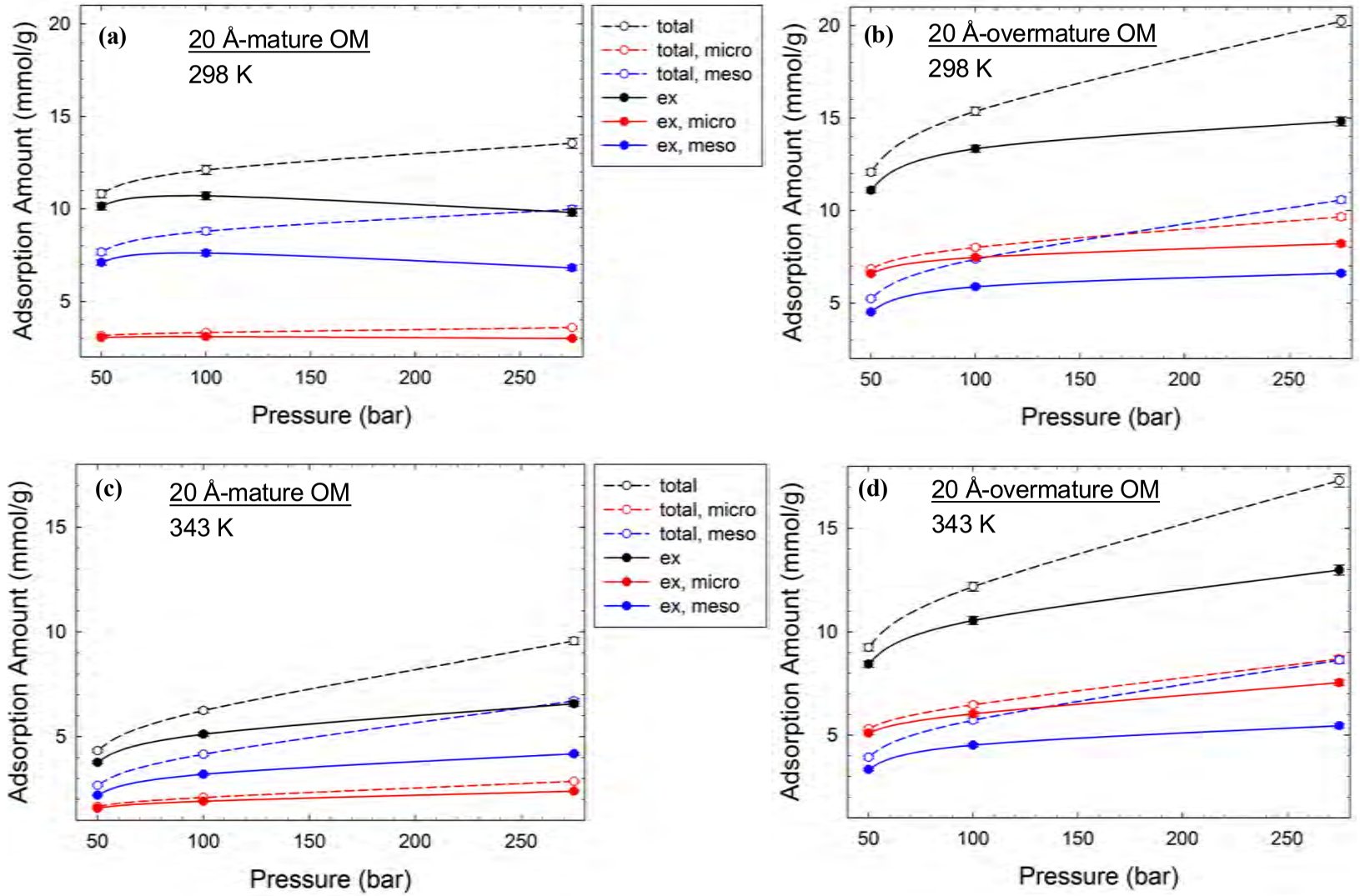

Figure 4: Adsorption isotherms of methane at temperatures of 298 and 343 K in the microporous and mesopore regions of the 20 Å-mature and 20 Å-overmature organic matter structures. The dashed lines and open symbols denote the total adsorption amount, while the solid lines and filled symbols correspond to the excess adsorption amount. The lines serve as a guide to the eye only.

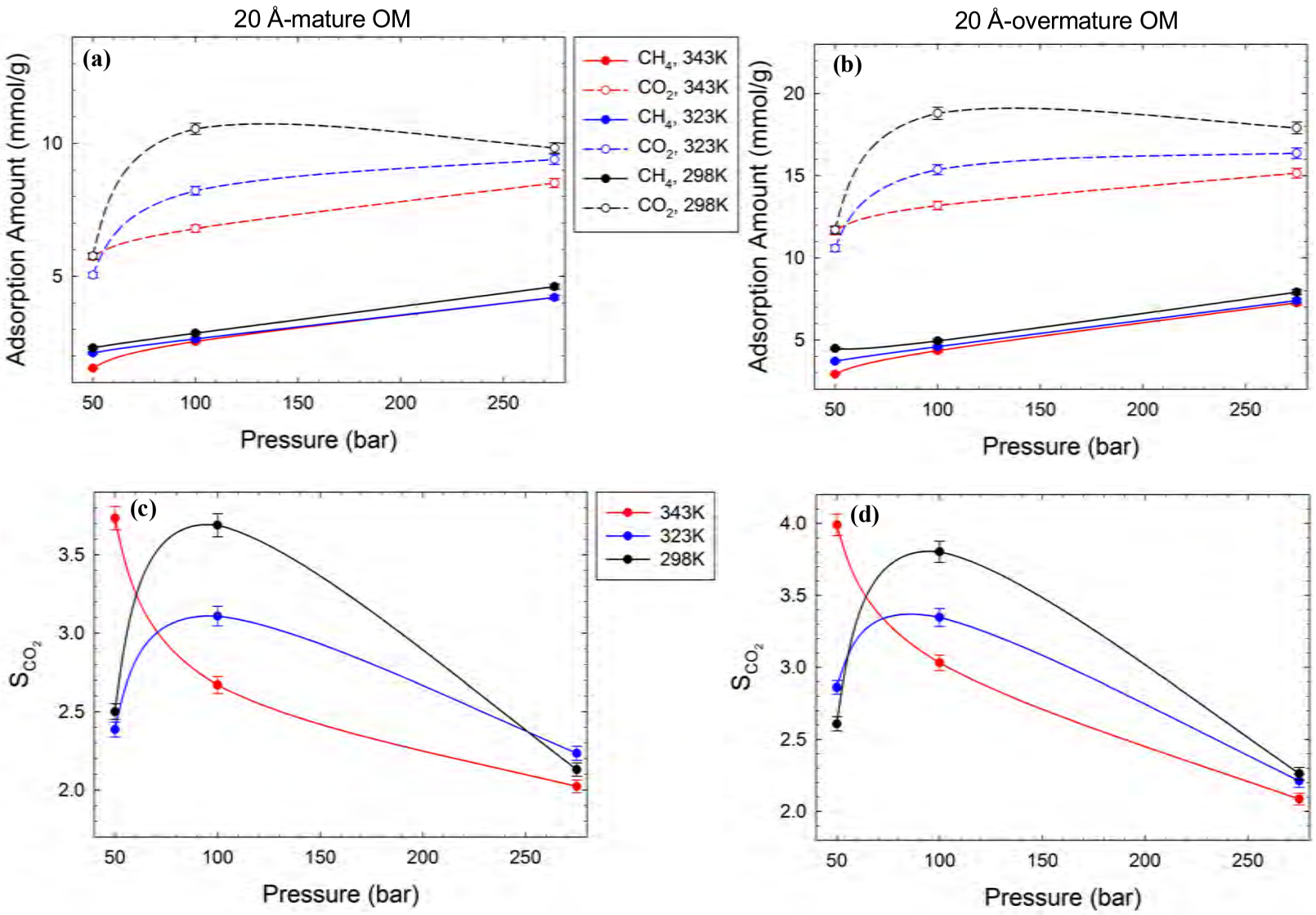

Figure 5: (a, b) Adsorption isotherms and (c, d) selectivity parameter, S_{CO_2}, of equimolar methane/carbon dioxide mixtures in the 20 Å-mature and 20 Å-overmature organic matter structures. The solid lines and filled symbols denote the results for methane, while the dashed lines and open symbols correspond to the results for carbon dioxide. The lines serve as a guide to the eye only.

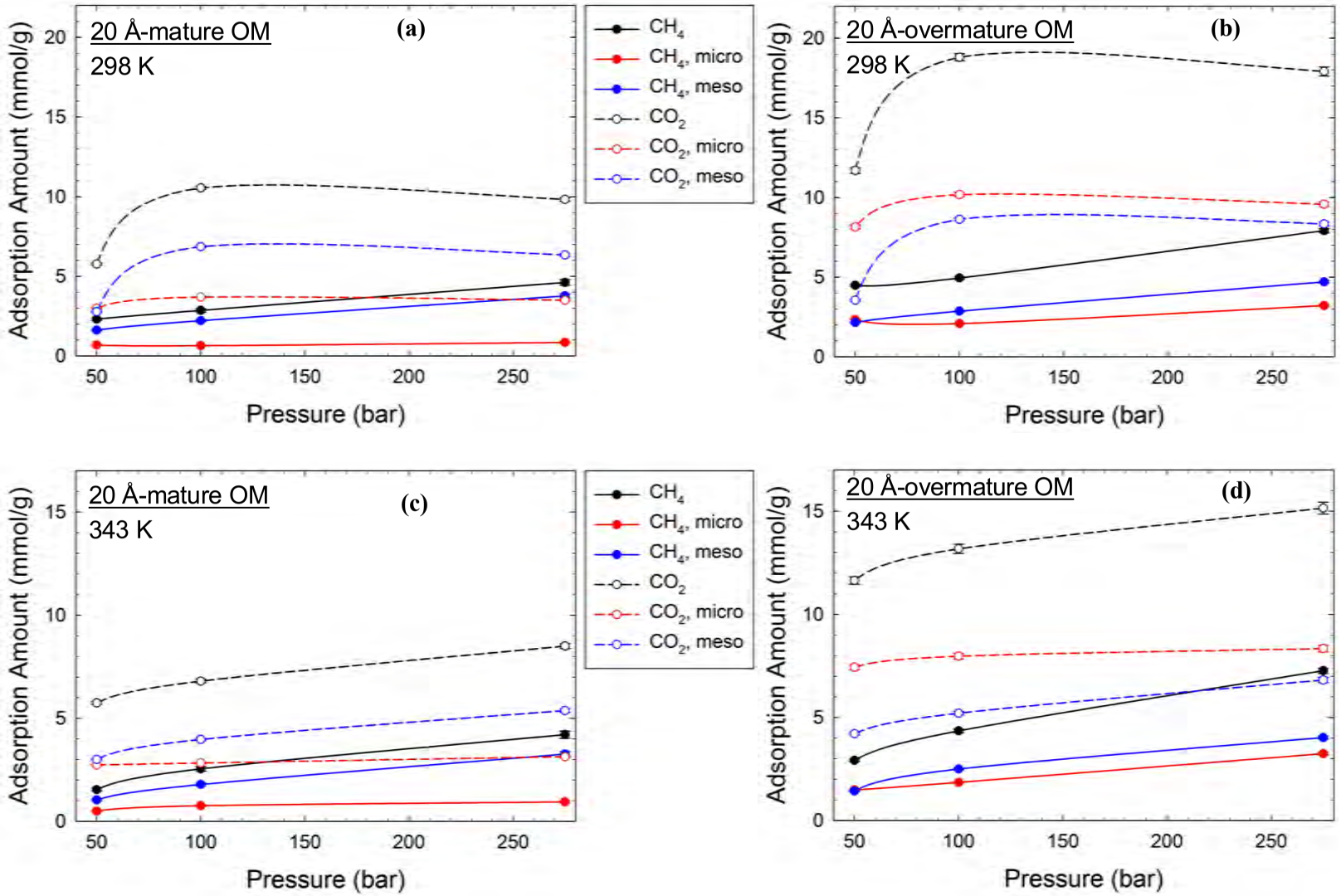

Figure 6: Adsorption isotherms of equimolar methane/carbon dioxide mixtures at temperatures of 298 and 343 K in the microporous and mesopore regions of the 20 Å-mature and 20 Å-overmature organic matter structures. The solid lines and filled symbols denote the results for methane, while the dashed lines and open symbols correspond to the results for carbon dioxide. The lines serve as a guide to the eye only.

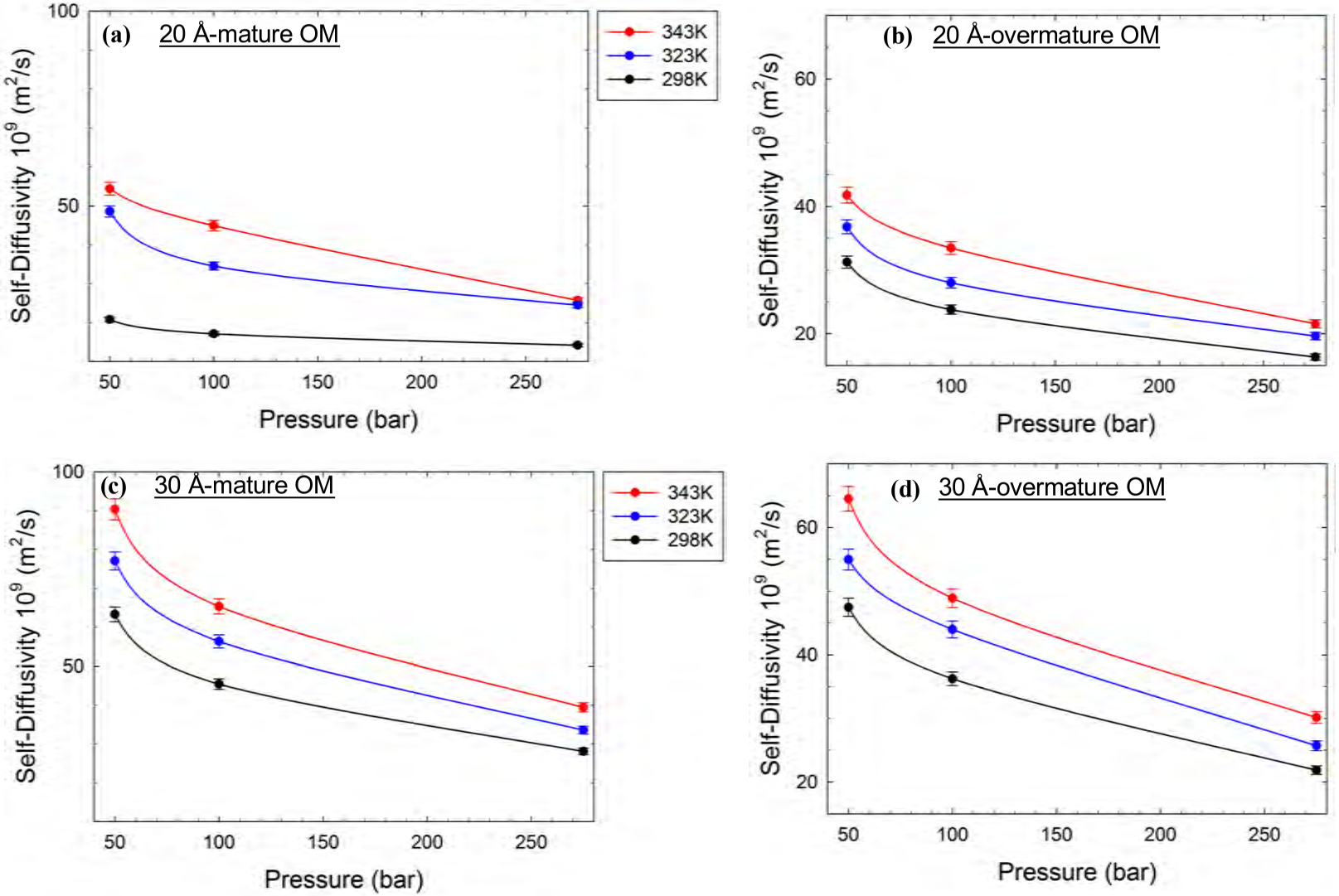

Figure 7: The self-diffusivity of methane along the adsorption isotherms in the mature and overmature organic matter structures. The lines serve as a guide to the eye only.

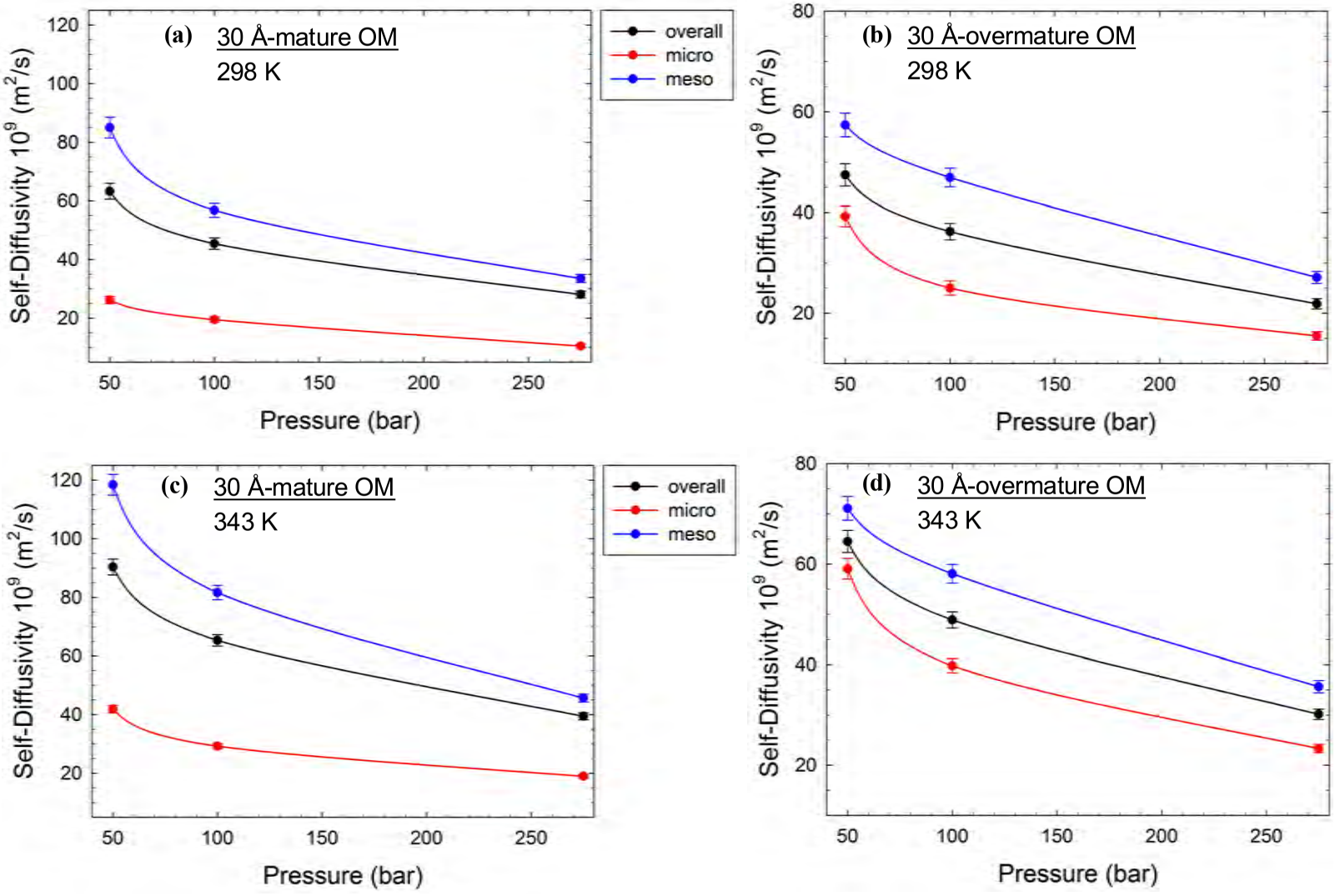

Figure 8: The self-diffusivity of methane along the adsorption isotherms at temperatures of 298 and 343 K in the microporous and mesopore regions of the 30 Å-mature and 30 Å-overmature organic matter structures. The lines serve as a guide to the eye only.

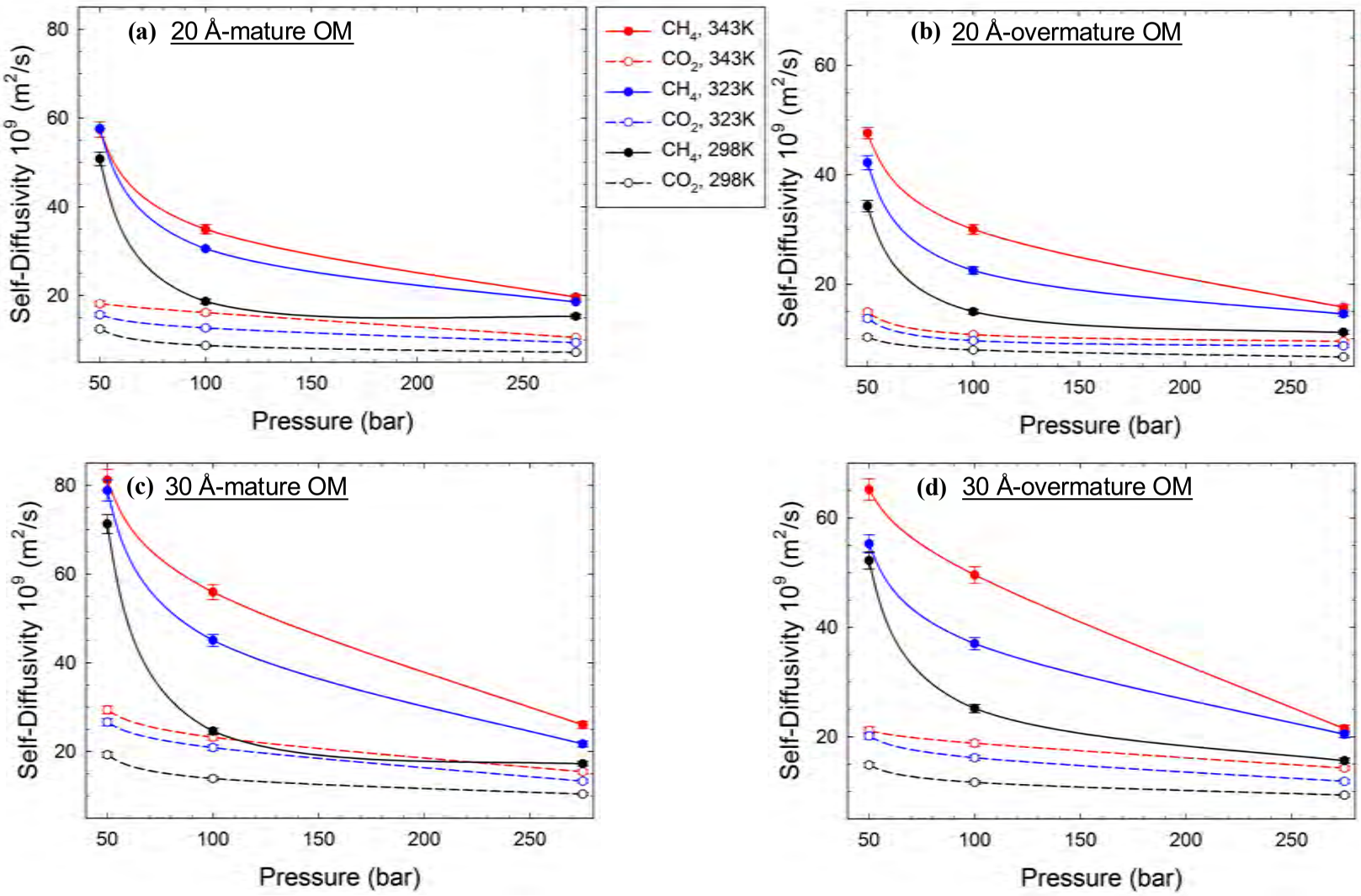

Figure 9: The self-diffusivity of methane and carbon dioxide along the mixture adsorption isotherms in the mature and overmature organic matter structures. The solid lines and filled symbols denote the results for methane, while the dashed lines and open symbols correspond to the results for carbon dioxide. The lines serve as a guide to the eye only.

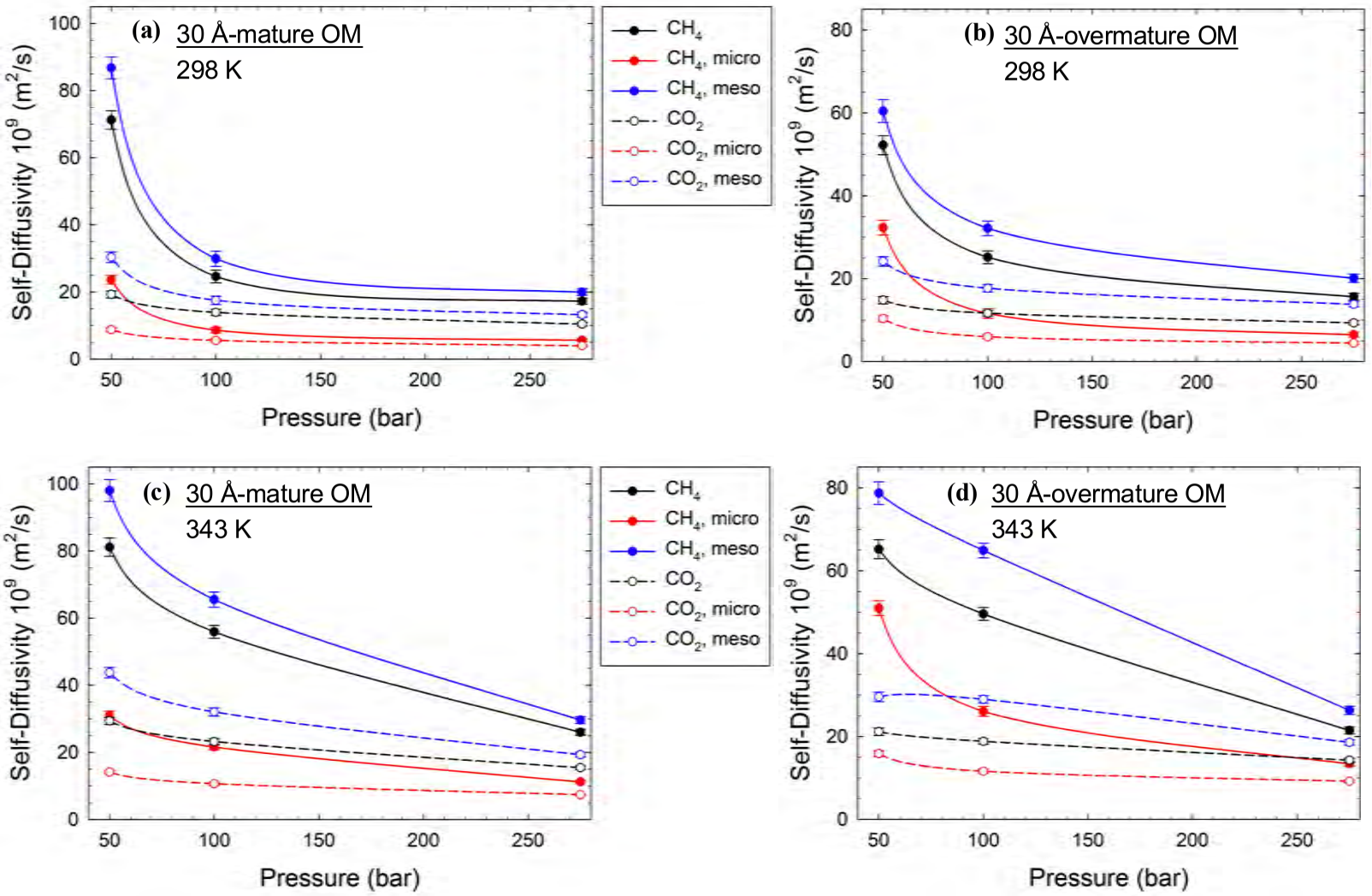

Figure 10: The self-diffusivity of methane and carbon dioxide along the mixture adsorption isotherms at temperatures of 298 and 343 K in the microporous and mesopore regions of the 30 Å-mature and the 30 Å-overmature organic matter structures. The solid lines and filled symbols denote the results for methane, while the dashed lines and open symbols correspond to the results for carbon dioxide. The lines serve as a guide to the eye only.

References

[1] Striolo, A., Cole, D.R., 2017. Understanding shale gas: Recent progress and remaining challenges. Energy Fuels 31, 10300-10310.

[2] Tissot, B.P., Welte, D.H. 1984, Petroleum Formation and Occurrence. Springer, Berlin.

[3] Michalec, L., Lísal, M., 2017. Molecular simulation of shale gas adsorption onto overmature type II model kerogen with control microporosity. Molec. Phys. 115, 1086-1103.

[4] Liu, D., Li, Y., Yang, S., Agarwal, R.K., 2019. CO_2 sequestration with enhanced shale gas recovery. Energ. Source. Part A. 41, 2975-2988.

[5] Qiao, S.Z., Bhatia, S.K., Nicholson, D., 2004. Study of hexane adsorption in nanoporous MCM-41 silica. Langmuir 20, 389-395.

[6] Luo, S., Nasrabadi, H., Lutkenhaus, J.L., 2016. Effect of confinement on the bubble points of hydrocarbons in nanoporous media. AIChE J. 62, 1772-1780.

[7] Zeigermann, P., Dvoyashkin, M., Valiullin, R., Kärger, J., Leipzig, U., 2009. Assessing the pore critical point of the confined fluid by diffusion measurement. Diffus. Fundam. 32, 41-58.

[8] Alfi, M., Nasrabadi, H., Banerjee, D., 2016. Experimental investigation of confinement effect on phase behavior of hexane, heptane and octane using lab-on-a-chip technology. Fluid Phase Equilib. 423, 25-33.

[9] Liu, X., Zhang, D., 2019. A review of phase behavior simulation of hydrocarbons in confined space: Implications for shale oil and shale gas. J. Nat. Gas Sci. Eng. 68, 102901.

[10] Wang, H., Qu, Z., Yin, Y. Bai, J., Yu, B., 2019. Review of molecular simulation method for gas adsorption/desorption and diffusion in shale matrix. J. Therm. Sci. 28, 1-16.

[11] Allen, M.P., Tildesley, D.J., 1987. Computer Simulation of Liquids. Clarendon Press, Oxford.

[12] Frenkel, D., Smit, B., 2002. Understanding Molecular Simulation. From Algorithms to Applications. Elsevier, Amsterdam.

[13] Lísal, M., Brennan, J.K., Smith, W.R., Siperstein, F.R., 2004. Dual control cell reaction ensemble molecular dynamics: A method for simulations of reactions and adsorption in porous materials, J. Chem. Phys. 121, 4901-4912.

[14] Van Krevelen, D.W., 1961. Coal: Typology, Chemistry, Physics, Constitution. Elsevier, Amsterdam.

[15] Seewald, J.S., 2003. Organic-inorganic interactions in petroleum-producing sedimentary basins. Nature 426, 327-333.

[16] Palmer, J.C., Gubbins, K.E., 2012. Atomistic models for disordered nanoporous carbons using reactive force fields. Microporous Mesoporous Mater. 154, 24-37.

[17] Mosher, K., He, J., Liu, Y., Rupp, E., Wilcox, J., 2013. Molecular simulation of methane adsorption in micro- and mesoporous carbons with applications to coal and gas shale systems. Int. J. Coal Geol. 109-110, 36-44.

[18] Kowalczyk, P., Gauden, P.A., Terzyk, A.P., Furmaniak, S., Harris, P.J.F., 2012. Displacement of methane by coadsorbed carbon dioxide is facilitated in narrow carbon nanopores. J. Phys. Chem. C 116, 13640-13649.

[19] Yuan, Q., Zhu, X., Lin, K., Zhao, Y.P., 2015. Molecular dynamics simulations of the enhanced recovery of confined methane with carbon dioxide. Phys. Chem. Chem. Phys. 17, 31887–31893.

[20] Van Duin, A.C., Dasgupta, S., Lorant, F., Goddard, W.A., 2001. ReaxFF: A reactive force field for hydrocarbons. J. Phys. Chem. A 105, 9396-9409.

[21] Ni, B., Lee, K.-H., Sinnott, S.B., 2004. A reactive empirical bond order (REBO) potential for hydrocarbon-oxygen interactions. J. Phys. Cond. Mater. 16, 7261-7275.

[22] Falk, K., Coasne, B., Pellenq, R., Ulm, F.-J., Bocquet, L., 2015. Subcontinuum mass transport of condensed hydrocarbons in nanoporous media. Nat. Commun. 6, 6949.

[23] Bousige, C., Ghimbeu, C.M., Vix-Guterl, C., Pomerantz, A.E., Suleimenova, A., Vaughan, G., Garbarino, G., Feygenson, M., Wildgruber, C., Ulm, F.-J., Pellenq, R.J.-M., Coasne, B., 2016. Realistic molecular model of kerogen's nanostructure. Nat. Mater. 15, 576-583.

[24] Ungerer, P., Collell, J., Yiannourakou, M., 2015. Molecular modeling of the volumetric and thermodynamic properties of kerogen: Influence of organic type and maturity. Energy Fuels 29, 91-105.

[25] Kelemen, S.R., Afeworki, M., Gorbaty, M.L., Sansone, M., Kwiatek, P.J., Walters, C.C., Freund, H., Siskin, M., Bence, A.E., Curry, D.J., Solum, M., Pugmire, R.J., Vandenbroucke, M., Leblond, M., Behar, F., 2007. Direct characterization of kerogen by X-ray and solid-state ^{13}C nuclear magnetic resonance methods. Energy Fuels, 21, 1548-1561.

[26] Vasileiadis, M., Peristeras, L.D., Papavasileiou, K.D., Economou I.G., 2017. Modeling of bulk kerogen porosity: Methods for control and characterization. Energy Fuels 31, 6004-6018.

[27] Obliger, A., Valdenaire, P.-L., Ulm, F.-J., Pellenq, R.J.-M., Leyssale, J.-M., 2019. Methane diffusion in a flexible kerogen matrix. J. Phys. Chem. B 123, 5635-5640.

[28] Obliger, A., Valdenaire, P.-L., Capit, N., Ulm, F.-J., Pellenq, R.J.-M., Leyssale, J.-M., 2018. Poroelasticity of methane-loaded mature and immature kerogen from molecular simulations. Langmuir 34, 13766-13780.

[29] Tesson, S., Firoozabadi, A., 2018. Methane adsorption and self-diffusion in shale kerogen and slit nanopores by molecular simulations. J. Phys. Chem. C 122, 23528-23542.

[30] Tesson, S., Firoozabadi, A., 2019. Deformation and swelling of kerogen matrix in light hydrocarbons and carbon dioxide. J. Phys. Chem. C 123, 29173-29183.

[31] Collell, J., Galliero, G., Vermorel, R., Ungerer, P., Yiannourakou, M., Montel, F., Pujol, M., 2015. Transport of multicomponent hydrocarbon mixtures in shale organic matter by molecular simulations. J. Phys. Chem. C 119, 22587-22595.

[32] Vasileiadis, M., Peristeras, L.D., Papavasileiou, K.D., Economou I.G., 2018. Transport properties of shale gas in relation to kerogen porosity. J. Phys. Chem. C 122, 6166–6177.

[33] Ho, T.A., Criscenti, L.J., Wang, Y., 2016. Nanostructural control of methane release in kerogen and its implications to wellbore production decline. Sci. Rep. 6, 28053.

[34] Sui, H., Yao, J., 2016. Effect of surface chemistry for CH_4/CO_2 adsorption in kerogen: A molecular simulation study. J. Nat. Gas Sci. Eng. 31, 738-746.

[35] Sun, H., Zhao, H., Qi, N., Li, Y., 2017. Molecular insights into the enhanced shale gas recovery by carbon dioxide in kerogen slit nanopores. J. Phys. Chem. C 121, 10233-10241.

[36] Wang, T., Tian, S., Li, G., Sheng, M., Ren, W., Liu,Q., Zhang, S., 2018. Molecular simulation of CO_2/CH_4 competitive adsorption on shale kerogen for CO_2 sequestration and enhanced gas recovery. J. Phys. Chem. C 122, 17009-17018.

[37] Ho, T.A., Wang, Y., 2019. Enhancement of oil flow in shale nanopores by manipulating friction and viscosity. Phys. Chem. Chem. Phys. 21, 12777-12786.

[38] Zhou, J., Jin, Z., Luo, K.H., 2019. Effects of moisture contents on shale gas recovery and CO_2 sequestration. Langmuir 35, 8716-8725.

[39] Lee, H., Shakib, F.A., Shokouhimehr, M., Bubach, B., Kong, L., Ostadhassan, M., 2019. Optimal separation of CO_2/CH_4/brine with amorphous kerogen: A thermodynamics and kinetics study. J. Phys. Chem. C 123, 20877-20883.

[40] Collell, J., Ungerer, P., Galliero, G., Yiannourakou, M., Montel, F., Pujol, M., 2014. Molecular simulation of bulk organic matter in type II shales in the middle of the oil formation window. Energy Fuels 28, 7457-7466.

[41] Rezlerová, E., Zukal, A., Čejka, J., Siperstein, F.R., Brennan, J.K., Lísal, M., 2017. Adsorption and diffusion of C_1 to C_4 alkanes in dual-porosity zeolites by molecular simulations. Langmuir 33, 11126-11137.

[42] Durand, B., 1980. Kerogen: Insoluble Organic Matter from Sedimentary Rocks. Technip, Paris.

[43] Lagache, M., Ungerer, P., Boutin, A., 2004. Prediction of thermodynamic derivative properties of natural condensate gases at high pressure by Monte Carlo simulation. Fluid Phase Equilib. 220, 211-223.

[44] Ungerer, P., Rigby, R., Leblanc, B., Yiannourakou, M., 2013. Sensitivity of the aggregation behaviour of asphaltenes to molecular weight and structure using molecular dynamics. Molec. Simul. 40, 115-122.

[45] Leach, A.R., 2001. Molecular Modelling: Principles and Applications. Pearson Prentice Hall, Upper Saddle River.

[46] Dauber-Osguthorpe, P., Roberts, V.A., Osguthorpe, D.J., Wolff, J., Genest, M., Hagler, A.T., 1988. Structure and energetics of ligand binding to proteins: Escherichia coli dihydrofolate reductase-trimethoprim, a drug-receptor system. Proteins 4, 31-47.

[47] Jorgensen, W.L., Maxwell, D.S., Tirado-Rives, J., 1996. Development and testing of the OPLS all-atom force field on conformational energetics and properties of organic liquids. J. Am. Chem. Soc. 118, 11225-11236.

[48] Cygan, R.T., Liang, J.-J., Kalinichev, A.G., 2004. Molecular models of hydroxide, oxyhydroxide, and clay phases and the development of a general force field. J. Phys. Chem. B 108, 1255-1266.

[49] Berendsen, H.J.C., Postma, J.P.M., van Gunsteren, W.F., Hermann, J., 1981. Intermolecular Forces. Reidel, Dordrecht.

[50] Harris, J.G., Yung, K.H., 1995. Carbon dioxide's liquid-vapor coexistence curve and critical properties as predicted by a simple molecular model. J. Phys. Chem. 99, 12021-12024.

[51] Chen, B., Siepmann, J.I., 1999. Transferable potentials for phase equilibria. 3. Explicit-hydrogen description of normal alkanes. J. Phys. Chem. B 103, 5370-5379.

[52] Potoff, J.J., Siepmann, J.I., 2001. Vapor-liquid equilibria of mixtures containing alkanes, carbon dioxide, and nitrogen. AIChE J. 47, 1676-1682.

[53] Svoboda, M., Lísal, M., 2018. Concentrated aqueous sodium chloride solution in clays at thermodynamic conditions of hydraulic fracturing: Insight from molecular dynamics simulations. J. Chem. Phys. 148, 222806.

[54] Widom, B., 1963. Some topics in the theory of fluids. J. Chem. Phys. 39, 2808-2812.

[55] Lísal, M., Předota, M., Brennan, J.K., 2013. Molecular-level simulations of chemical reaction equilibrium and diffusion in slit and cylindrical nanopores: Model dimerisation reactions. Molec. Simul. 39, 1103-1120.

[56] Svoboda, M., Brennan, J.K., Lísal, M., 2015. Molecular dynamics simulation of carbon dioxide in single-walled carbon nanotubes in the presence of water: Structure and diffusion studies. Molec. Phys. 113, 1124-1136.

[57] Greathouse, J.A., Hart, D.B., Bowers, G.M., Kirkpatrick, R.J., Cygan, R.T., 2015. Molecular simulation of structure and diffusion at smectite-water interfaces: Using expanded clay interlayers as model nanopores. J. Phys. Chem. C 119, 17126-17136.

[58] Montgomery, S.L., Jarvie, D.M., Bowker, K.A., Pollastro, R.M., 2005. Mississippian Barnett shale, Fort Worth basin, north-central Texas: Gas-shale play with multi-trillion cubic foot potential. AAPG Bull. 89, 155-175.

[59] NIST webbook: Thermophysical Properties of Fluid Systems, http://webbook.nist.gov/chemistry/fluid.

[60] Gelb, L.D., Gubbins, K.E., 1999. Pore size distributions in porous glasses: A computer simulation study. Langmuir 15, 305-308.

[61] Sarkisov, L., Harrison, A., 2011. Computational structure characterisation tools in application to ordered and disordered porous materials. Molec. Simul. 37, 1248-1257.

[62] Lourenço, T.C., Coelho, M.F.C., Ramalho, T.C., van der Spoel, D., Costa, L.T., 2013. Insights on the solubility of CO_2 in 1-ethyl-3-methylimidazolium bis(trifluoromethylsulfonyl)imide from the microscopic point of view. Environ. Sci. Technol. 47, 7421-7429.

[63] Huang, L., Ning, Z., Wang, Q., Zhang, W., Cheng, Z., Wu, X., Qin, H., 2018. Effect of organic type and moisture on CO_2/CH_4 competitive adsorption in kerogen with implications for CO_2 sequestration and enhanced CH_4 recovery. Appl. Energy 210, 28-43.

[64] Zhang, J., Liu, K., Clennell, M., Dewhurst, D., Pervukhina, M., 2015. Molecular simulation of CO_2-CH_4 competitive adsorption and induced coal swelling. Fuel 160, 309-317.